Molecular and Electronic Structure in the Metal-to-Ligand Charge Transfer Excited States of *fac*-[Re(4,4′-X_2bpy)$(CO)_3$(4-Etpy)]$^{+}$* (X = CH_3, H, Co_2Et). Application of Density Functional Theory and Time-Resolved Infrared Spectroscopy

Dana M. Dattelbaum,*,† Richard L. Martin,*,‡ Jon R. Schoonover,† and Thomas J. Meyer§

Materials Science and Technology and Theoretical Divisions and the Associate Laboratory Director's Office for Strategic Research, Los Alamos National Laboratory, Los Alamos, New Mexico 87545

Received: October 13, 2003; In Final Form: January 20, 2004

Density functional theory (DFT) calculations have been conducted on the ground and metal-to-ligand charge transfer (MLCT) excited states of the series *fac*-[Re(4,4′−X_2bpy)$(CO)_3$(4-Etpy)](PF_6) (X = CH_3, H, and CO_2Et; 4-Etpy is 4-ethylpyridine). The energy gap varies across this series, influencing excited-state geometries and electronic structures. The DFT calculations assist in assigning ν(CO) bands in the infrared and give insight into variations in the experimental values. The predicted bond length and angle changes in the excited state point to the importance of Re−CO σ bond polarization in the excited states as well as π^*(4,4′−X_2-bpy)−π^*(CO) mixing suggested previously.

Introduction

The properties of metal-to-ligand charge transfer (MLCT) excited states of ruthenium(II) and osmium(II) have begun to be exploited systematically in sensing, electron and chemiluminescence, and light-to-energy conversion devices. MLCT excited states based on rhenium(I) also hold potential for such applications. The sensitivity of their photophysical properties to the environment makes them ideal candidates as sensors of local microscopic environmental conditions, such as polarity, pH, CO_2, and O_2.[1−7]

In the series $[(pp)Re^{I}(CO)_3(L)]^{n+}$ (where pp is a bidendate polypyridyl ligand such as 2,2′-bipyridine or 1,10-phenanthroline and L is an ancillary ligand such as Cl^- or 4-ethylpyridine; n = 0 or 1), intense MLCT absorptions appear in the high energy visible region that are easily tunable by substitution at the polypyridyl (pp) or ancillary (L) ligands based on well-established synthetic methodologies. The excited states of a series of complexes have been examined where the ground-to-excited-state energy gap, E_0, is varied by ligand substitution at the 4- and 4′-positions on 2,2′-bipyridine in *fac*-[Re(4,4′−X_2-bpy)$(CO)_3$(4-Etpy)](PF_6) (X = CH_3, H, and CO_2Et; 4-Etpy is 4-ethylpyridine).[8] In this series, E_0 increases in the order 4,4′-$(CO_2Et)_2$bpy < bpy < 4,4′-$(CH_3)_2$bpy. To better understand the molecular and electronic structures of the ground and excited states of these complexes, we have coupled density functional theory (DFT) calculations with time-resolved infrared (TRIR) studies.

Excited states of the series *fac*-$[Re(pp)(CO)_3(L)]^{n+}$ were among the first to be characterized by time-resolved infrared spectroscopy due to the high oscillator strengths of the carbonyl ligands and the ease of measurement of ν(CO) bands in the 1800−2200 cm^{-1} spectral region.[9−17] TRIR measurements have been used to map MLCT excited states localized on the polypyridyl ligand, eq 1.

$$[(bpy)Re^{I}(CO)_3(4\text{-Etpy})]^{+} \underset{^1(d\pi^6)}{=} \xrightarrow{h\nu} [(bpy^{\bullet -})Re^{II}(CO)_3(4\text{-Etpy})]^{+} \underset{d\pi^5\pi^{*1}}{} \quad (1)$$

The thermally relaxed excited states that form following MLCT singlet excitation and nonradiative decay are a manifold of three, Boltzmann populated states largely triplet in character, split from the parent triplet by low symmetry and spin−orbit coupling.[18−20] In this largely triplet "excited state", the ν(CO) bands increase in energy by 50−100 cm^{-1} compared to the ground state. These shifts are due to the change in electronic configuration from $d\pi^6$ to $d\pi^5\pi^{*1}$, eq 1, which decreases electron density at the metal and with it, $d\pi$(Re)−π^*(CO) back-bonding.

The energy factored force field approach has often been applied to transition metal carbonyl complexes to approximate carbonyl force constants[21] in ground and excited states.[22−24] DFT calculations have also been successful in tracking experimental frequencies measured by time-resolved vibrational measurements.[25−32] In the present study, the DFT calculations provide the basis for both assignments and band shifts in the MLCT excited state of the series of complexes where the energy gap is varied. In addition to assisting in vibrational assignments, the calculations provide additional structural information about the MLCT excited state.

Experimental Section

Materials. Acetonitrile was obtained from Aldrich and used without further purification. *Fac*-[Re(4,4′-$(CH_3)_2$bpy)$(CO)_3$(4-Etpy)](PF_6), *fac*-[Re(bpy)$(CO)_3$(4-Etpy)](PF_6), and *fac*-[Re(4,4′-$(CO_2Et)_2$bpy)$(CO)_3$(4-Etpy)](PF_6) (4-Etpy is 4-ethylpyridine) were prepared according to literature procedures.[33,34] Tetra-*n*-butylammonium hexafluorophosphate (TBAH) was obtained from Aldrich and recrystallized twice from ethanol before use.

* Corresponding authors.
† Materials Science and Technology Division, Los Alamos National Laboratory.
‡ Theoretical Division, Los Alamos National Laboratory.
§ Associate Laboratory Director's Office for Strategic Research, Los Alamos National Laboratory.

10.1021/jp037095m CCC: $27.50
Published on Web 03/23/2004

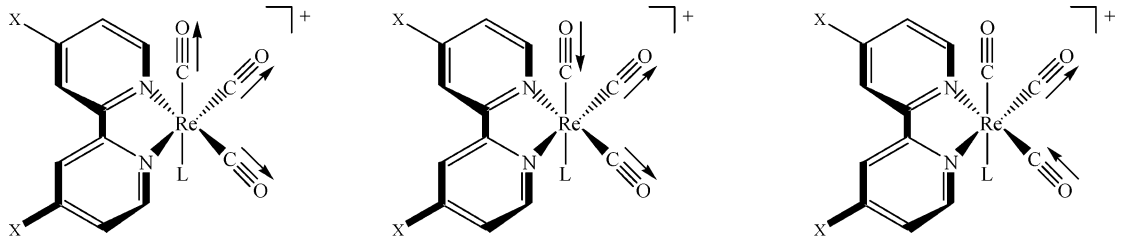

A'(1) **A'(2)** **A''**

Figure 1. A′(1), A′(2), and A″ normal modes in C_s symmetry for [$Re^{II}(pp^{\bullet-})(CO)_3$(4-Etpy)]$^{+}$*.

TABLE 1: Ground- ($\bar{\nu}_{gs}$) and Excited-State ($\bar{\nu}_{es}$) Infrared Band Energies (±2 cm^{-1}) and Ground (gs)-to-Excited State (es) Shifts ($\Delta\bar{\nu} = \bar{\nu}_{es} - \bar{\nu}_{gs}$) for *fac*-[Re(4,4′-$X_2$bpy)$(CO)_3$(4-Etpy)]$^{+}$ in Acetonitrile at 298 K[a]

	$\Delta\bar{\nu}$ (cm^{-1})			$\bar{\nu}_{gs}$ (cm^{-1})		$\bar{\nu}_{es}$ (cm^{-1})		
complex[b]	A″	A′(2)	A′(1)	A″, A′(2)	A′(1)	A″	A′(2)	A′(1)
[Re(4,4′-$(CH_3)_2$bpy)$(CO)_3$(4-Etpy)]$^{+}$	37	81	33	1927	2034	1964	2008	2067
	21	*42*	*12*	*2035, 2046*	*2117*	*2056*	*2088*	*2129*
[Re(bpy)$(CO)_3$(4-Etpy)]$^{+}$	44	83	39	1927	2035	1971	2010	2074
	22	*44*	*15*	*2038, 2049*	*2120*	*2060*	*2093*	*2135*
[Re(4,4′-$(CO_2Et)_2$bpy)$(CO)_3$(4-Etpy)]$^{+}$	45	88	54	1933	2038	1978	2023	2092
	22	*45*	*21*	*2040, 2051*	*2120*	*2062*	*2096*	*2141*

[a] The second row in italics gives the density functional theory results for comparison. [b] As PF_6^- salts.

Emission Spectra. Corrected emission spectra were recorded on a SPEX Fluorolog-2 emission spectrometer equipped with a 450 W Xe lamp and cooled 10-stage Hammamatsu R928 or R664 photomultipliers. The response from the photomultipliers was corrected with a calibration curve generated with 1.0 mm slits by using a NIST-calibrated standard lamp (Optronics Laboratories, Inc. Model 220 M) controlled by a precision current source at 6.50 W (Optronics Laboratories, Inc. Model 65). All spectra were acquired in acetonitrile solution at room temperature in 1 cm path length quartz cells (o.d. < 0.05) by using right-angle observation of the emitted light.

Time-Resolved Infrared Spectroscopy. The infrared beam from a Bruker IFS 66V/s spectrometer was directed through a BaF_2 window contained in a flange in the front of the bench by using an optional computer driven mirror. The beam was then directed by a gold-coated mirror and focused onto the sample by a BaF_2 lens. After the sample, the diverging beam was recollimated and focused onto the detector element of a Kolmar liquid N_2-cooled MCT photovoltaic detector fitted with a fast 50 MHz preamplifier. A 354.7 nm pump beam from a Surelite Continuum Nd:YAG laser operating at 10 Hz was focused, directed onto the sample and overlapped with the infrared beam using a pinhole aperture. The external optical train was enclosed in a plexiglass box continuously purged with dry N_2. Both the detector and sample were mounted on *x*, *y*, and *z* translational stages for maximum alignment. A Stanford Research Systems model DG535 pulse generator controlled experimental timing of the laser pulse and interferometer mirror step.

In our experimental configuration, an AC rapid scan single channel spectrum was taken prior to commencement of the step-scan experiment and was used as the ground state spectrum. Time-resolved infrared spectra were recorded in step-scan mode by using the PAD 82a transient ADC board. The AC signal from the MCT detector was fed into channel A on a PAD 82a transient digitizer board. The DC signal was fed into channel B and used for phase correction. Channel C received a trigger signal to initiate data collection. Signal intensities were collected in 20 or 50 ns time increments for approximately 600 ns. In step coadditions (64−180) were used to increase the signal-to-noise ratio. Following the completion of an experiment, interferograms were Fourier transformed and sorted in time producing a 3D data set of single channel spectra. This 3D file was further manipulated by a macro that converted the single channel spectra into absorption difference spectra by using the relationship defined in Chen et al.[35] Time slices following the laser pulse were also signal averaged over the lifetime of the excited state.

Samples for TRIR Studies. All infrared spectra were measured in acetonitrile solutions, in 0.75 or 1 mm path length CaF_2 or BaF_2 liquid IR cells. Sample concentrations were adjusted to give an absorbance value of about 0.7 for the ν(CO) bands. The sample cell and sample solutions were deoxygenated by sparging with argon for 15 min and the solutions transferred to the cell under an inert atmosphere. Spectra were acquired in two blocks of 64 to prevent sample decomposition and averaged to give the final spectra.

DFT Calculations. The hybrid B3LYP DFT approximation,[36] as implemented in the G98 package,[37] was used to determine the geometries and associated energies of the ground state, a singlet, and lowest excited state, a triplet. The metal centers were described by the "small core" LANL2 relativistic effective core potential[38] and the associated basis set. The latter was completely uncontracted, except that for the resulting two primitive p functions with exponents 0.4960 and 0.4644, only the latter was retained in order to avoid linear dependency. This approach results in a (5s5p3d) basis for the metal. The 6-31G* basis set was used for the ligand atoms.

Results

The ground-state geometry of *fac*-[Re(bpy)$(CO)_3$(4-Etpy)]$^{+}$ is depicted in Figure 1. There is a mirror plane including the axial carbonyl and the metal center that bisects the two equatorial carbonyls and the polypyridyl ligand. There are three ν(CO) bands defined in C_s symmetry as two A′ modes and one A″ mode. Their local mode compositions are shown in Figure 1.

Table 1 lists the ground and excited-state band energies for the three ν(CO) modes for the series *fac*-[Re(4,4′−X_2bpy)$(CO)_3$-(4-Etpy)](PF_6) (X = CH_3, H, CO_2Et) in acetonitrile. Bands for all three modes are observed in the triplet excited state, but only two bands are resolved in the ground state. The broad band at lower energy observed in the ground-state spectrum is due to the overlapping A″, A′(2) modes. The predicted energy ordering is A′(1) > A′(2) > A″.

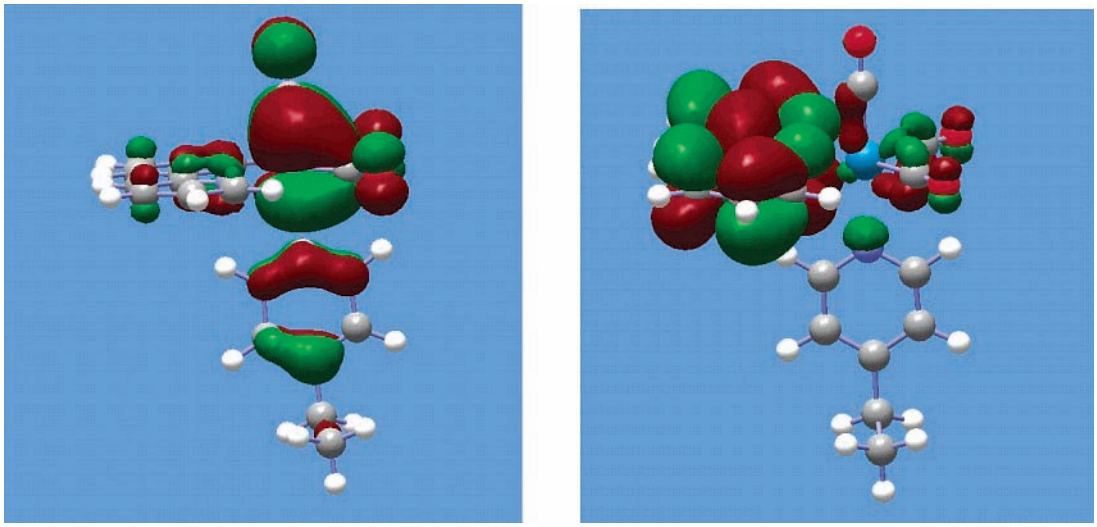

Figure 2. HOMO (left) and LUMO (right) orbitals as calculated by the use of density functional theory for the ground state *fac*-[Re(bpy)$(CO)_3$-(4-Etpy)]$^+$.

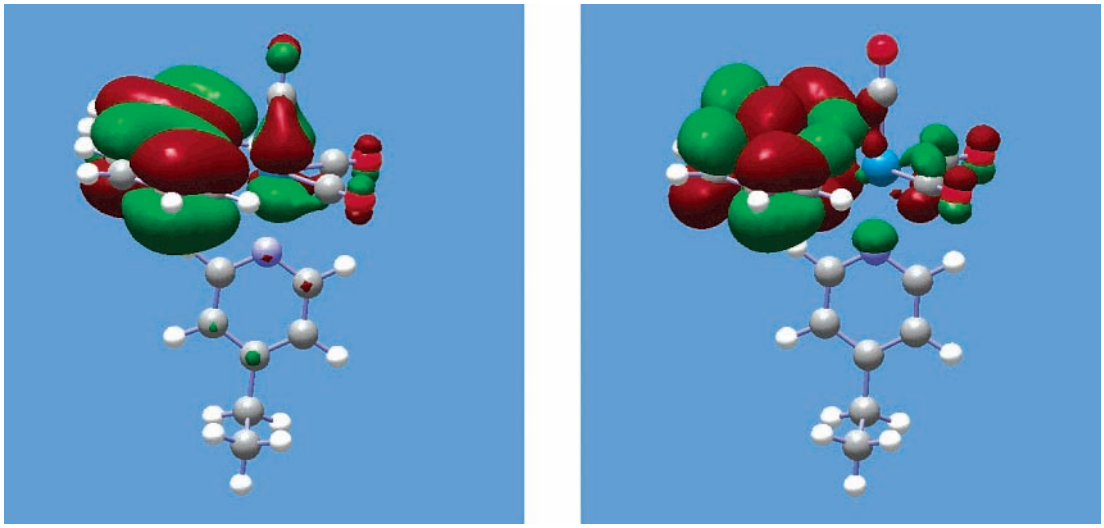

Figure 3. HOMO (left) and LUMO (right) orbitals for the metal-to-ligand charge-transfer excited state *fac*-[Re^{II}(bpy$^{\bullet-}$)$(CO)_3$(4-Etpy)]$^+$*.

TABLE 2: Vertical Absorption (ΔE_{vert}(S→T)), Emission, (ΔE_{vert}(T→S)) and Vibrational Relaxation (ΔE_{relax}(T)) Energies (in eV) Associated with the Lowest Excited Triplet State for [Re(4,4′−X_2bpy)$(CO)_3$(4-Etpy)]$^+$ [a]

complex[b]	ΔE_{vert} (S→T)	ΔE (S→T)	ΔE_{vert} (T→S)	ΔE_{relax} (T)[c]	ΔE_0(S→T) (ZPE corr)	E_0(expt)[b]	S[d]	E_{em}(expt)	μ (D)
[Re(4,4′-$(CH_3)_2$bpy)$(CO)_3$(4-Etpy)]$^+$	2.94	2.52	2.10	0.43	2.41	2.32	1.4	2.29	10.82 6.46
[Re(bpy)$(CO)_3$(4-Etpy)]$^+$	2.90	2.49	2.02	0.42	2.38	2.22	1.1	2.17	10.45 6.27
[Re(4,4′-$(CO_2Et)_2$bpy)$(CO)_3$(4-Etpy)]$^+$	2.73	2.37	2.01	0.37	2.26	2.01	1.0	1.98	8.24 7.19

[a] S and T refer to the singlet and triplet states, respectively. The zero point energy (ZPE) corrected energy gap, ΔE(S→T), and experimental energy gap (E_0) and emission energy (E_{em}) are included for comparison. The last column shows computed dipole moments (in Debye) of the singlet (first entry) and triplet (second entry) relative to the center of mass of the complex. [b] As PF_{6-} salts in CH_3CN at 298 K. [c] Vibrational relaxation energy in the excited triplet state. [d] Values were obtained using an in-house spectral fitting program described previously.[47] $\hbar\omega$ was fixed at 1450 cm^{-1} in the fits. E_0 includes the solvent reorganization energy difference between ground and excited states and low-frequency modes treated classically.

Ground-to-excited-state shifts, $\Delta\bar{\nu} = \bar{\nu}_{es} - \bar{\nu}_{gs}$, for the three ν(CO) bands are listed in Table 1. Figures 2 and 3 are depictions of the HOMO (highest occupied molecular orbital) and LUMO (lowest unoccupied molecular orbital) for both the ground and MLCT excited states. The metal-based HOMO in the ground-state transforms as a″ and the bipyridyl-based LUMO as a′. The excited triplet state is of a′ symmetry.

The $\nu = 0 \rightarrow \nu' = 0$ ground-to-excited-state energy gap, E_0, the electron-vibrational coupling constant (Huang−Rhys factor), S (derived by using a single-mode Franck−Condon analysis of emission spectral profiles), and the emission energy, E_{em}, are listed in Table 2.[47] There are several DFT entries in Table 2. From separate self-consistent field (SCF) calculations on the lowest singlet and triplet state at the optimal geometry of the singlet, we extracted the vertical absorption energy ΔE_{vert}(S→T). Similarly, from the separate SCF calculations at the optimal geometry of the triplet state, we report an analogous emission energy ΔE_{vert}(T→S). S and T refer to the singlet and triplet

TABLE 3: Calculated Parameters for the *ν*(CO) Vibrational Modes in *fac*-[Re(bpy)$(CO)_3$(4-Etpy)]$^+$

mode	$\bar{\nu}$ (cm^{-1})	μ (amu)	k (mdyn/Å)	I_{ir} (KM/mol)
		Ground State		
A′(1)	2120	13.28	35.15	843.2 (0.92)
A′(2)	2049	13.34	33.0	901.1 (0.98)
A″	2038	13.31	32.57	917.5 (1.00)
		^{3}MLCT		
A′(1)	2135	13.34	35.83	1312.1 (1.00)
A′(2)	2093	13.36	34.47	894.6 (0.68)
A″	2060	13.35	33.37	678.3 (0.52)

[a] Relative IR intensities are given parenthetically in the last column. μ and k are the reduced mass and force constant, respectively.

TABLE 4: Calculated Parameters[a] for the *ν*(CO) Vibrational Modes in *fac*-[Re(4,4′-$(CH_3)_2$bpy)$(CO)_3$(4-Etpy)]$^+$

mode	$\bar{\nu}$ (cm^{-1})	μ (amu)	k (mdyn/Å)	I_{ir} (KM/mol)
		Ground State		
A′(1)	2117	13.28	35.07	868.6 (0.93)
A′(2)	2046	13.34	32.89	911.1 (0.97)
A″	2035	13.31	32.48	933.2 (1.00)
		^{3}MLCT		
A′(1)	2129	13.34	35.61	1474.1 (1.00)
A′(2)	2088	13.36	34.32	930.7 (0.63)
A″	2056	13.35	33.24	641.3 (0.44)

[a] Relative IR intensities are given parenthetically in the last column. μ and k are the reduced mass and the force constant, respectively.

TABLE 5: Calculated Parameters[a] for the *ν*(CO) Vibrational Modes in *fac*-[Re(4,4′-$(CO_2Et)_2$bpy)$(CO)_3$(4-Etpy)]$^+$

mode	$\bar{\nu}$ (cm^{-1})	μ (amu)	k (mdyn/Å)	I_{ir} (KM/mol)
		Ground State		
A′(1)	2120	13.28	35.15	968.18 (1.00)
A′(2)	2051	13.34	33.06	896.85 (0.93)
A″	2040	13.31	32.62	927.54 (0.96)
		^{3}MLCT		
A′(1)	2141	13.34	36.06	1282.9 (1.00)
A′(2)	2096	13.36	34.58	938.6 (0.73)
A″	2062	13.35	33.44	619.1 (0.48)

[a] Relative IR intensities are given parenthetically in the last column. μ and k are the reduced mass and the force constant, respectively.

states, respectively. These entries do not include zero point energy (ZPE) correction (except where noted). The adiabatic excitation energy, ΔE(S→T), determined from the total energies, each at their respective geometry, is listed in column 3. The difference between the vertical and adiabatic S → T excitation energies allow us to infer the vibrational relaxation energy associated with the triplet reported in column 5. Finally, the adiabatic excitation energy was corrected for the ZPE contribution using the computed ZPE of 10.647 eV for the singlet and 10.537 eV for the excited-state triplet of [Re(4,4′-$(CH_3)_2$bpy)$(CO)_3$(4-Etpy)]$^+$, 9.146 eV for the singlet and 9.033 eV for the excited-state triplet of [Re(bpy)$(CO)_3$(4-Etpy)]$^+$, and 13.026 eV for the singlet and 12.921 eV for the excited-state triplet of [Re(4,4′-$(CO_2Et)_2$bpy)$(CO)_3$(4-Etpy)]$^+$. The experimental energy gaps and emission energies are included in the table for comparison.

The DFT calculated energy differences are gas-phase values. As noted below, the experimental energy gap derived by emission spectral fitting is a solution quantity and includes the solvent reorganization energy (λ_o) and the reorganization energy contributed by low frequency modes treated classically ($\lambda_{i,L}$). It is related to the free energy of the excited state above the ground state by, $\Delta G^\circ = E_0 - \lambda_0 - \lambda_{i,L}$.

Tables 3−5 list calculated ν(CO) parameters for each complex in the series. Included in tables are the band energy (cm^{-1}), reduced mass, μ(amu), force constants, k (mdyn/Å), and relative infrared intensities, I_{ir} (KM/mol). Table 6 lists calculated structural parameters for both ground and lowest MLCT excited-state geometries in the B3LYP approximation. Figure 4 is a schematic energy level diagram demonstrating the mixing that occurs between the lowest π^* orbital on the bpy acceptor ligand and the in-plane π^* carbonyl orbitals in the MLCT excited state. Figure 5 compares the experimental and calculated band energies through the series of complexes as a function of energy gap.

Discussion

TRIR Data. In a previous paper, we described a time-resolved infrared (TRIR) study of the metal-to-ligand charge transfer (MLCT) excited states of the two series, *fac*-[Re(pp)$(CO)_3$(4-Etpy)]$^+$ (pp = phen, bpy, 4,4′-$(CH_3)_2$bpy, 4,4′-$(CH_3O)_2$-bpy, or 4,4′-$(CO_2Et)_2$bpy; 4-Etpy = 4-ethylpyridine) and *cis*-[Os(pp)$_2$(CO)(L)]$^{n+}$ (pp = 1,10-phenanthroline (phen) or 2,2′-bipyridine (bpy); L = PPh_3, CH_3CN, pyridine, Cl, or H).[8] Time-resolved infrared spectra in the ν(CO) region revealed systematic variations in excited-state electronic structure as the ground-to-excited-state energy gap, E_0, was varied.

The TRIR results reported here are from measurements on the lowest excited triplet state with the hole in the dπ orbital, dπ_3. As noted in the Introduction, this lowest "state" is actually a manifold of three closely lying states, largely triplet in character, arising from a splitting of the lowest triplet state by low symmetry and spin−orbit coupling.[18−20]

There are two higher lying triplet manifolds in which the hole resides in the dπ_1 and dπ_2 levels. Preliminary time-dependent DFT (TDDFT) calculations suggest that the three triplets are reasonably well separated in energy. The calculations predict vertical gas-phase emission energies for *fac*-[Re(bpy)$(CO)_3$(4-Etpy)]$^+$ at 1.73, 2.17, and 2.31 eV from the three states at the equilibrium geometry of the lowest triplet. The experimental

TABLE 6: Bond Lengths (Å) and Angles (deg) in the B3LYP Approximation for the Ground State and Lowest MLCT Excited State of [Re(4,4′-X_2bpy)$(CO)_3$(4-Etpy)]$^+$[a]

	[Re(4,4′$(CH_3)_2$bpy)$(CO)_3$(4-Etpy)]$^+$		[Re(bpy)$(CO)_3$(4-Etpy)]$^+$		[Re(4,4′$(CO_2Et)_2$bpy)$(CO)_3$(4-Etpy)]$^+$	
	ground (Å or deg)	MLCT (Å or deg)	ground (Å or deg)	MLCT (Å or deg)	ground (Å or deg)	MLCT (Å or deg)
R(Re−CO_{ax})	1.940	1.992	1.941	1.997	1.943	2.002
R(Re−CO_{eq})	1.936	1.981, 1.977	1.936	1.980	1.938	1.980, 1.986
R(CO_{ax})	1.157	1.147	1.156	1.146	1.156	1.145
R(CO_{eq})	1.160	1.154	1.159	1.153	1.159	1.153
R(Re−N_{bpy})	2.204	2.117, 2.2124	2.205	2.124	2.201	2.127, 2.117
R(Re−N_{4-Etpy})	2.269	2.226	2.265	2.218	2.267	2.215
CO_{eq}−Re−CO_{eq}	90.97	87.05	90.90	86.79	91.05	86.64
CO_{ax}−Re−CO_{eq}	90.38, 90.46	91.44, 91.73	90.49, 90.3	91.86, 91.43	90.38, 90.29	91.29, 91.81

[a] With the present basis set, calculated R(CO) in free CO is 1.138 Å compared to the experimental value of 1.143 Å.[40]

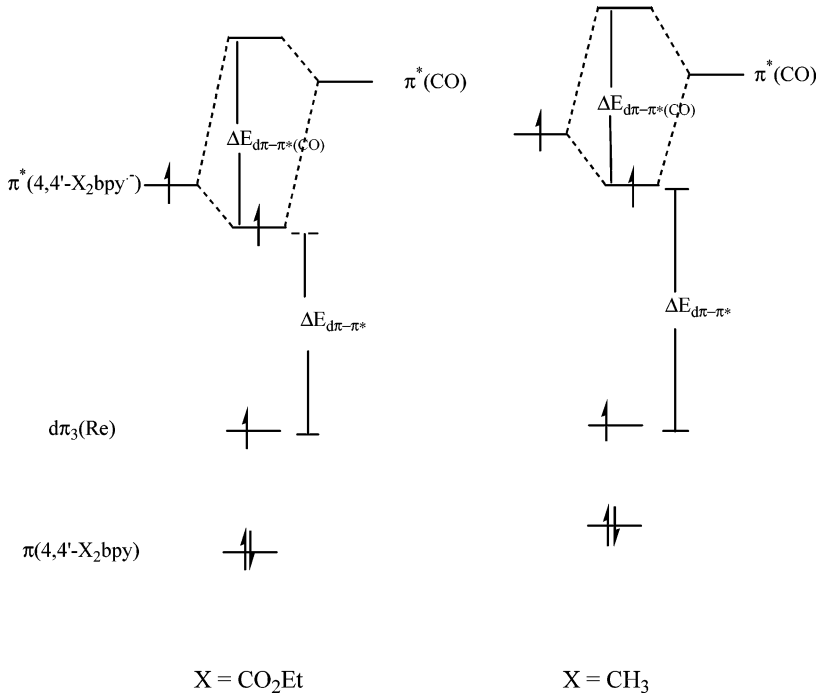

Figure 4. Schematic energy level diagram demonstrating the mixing between the lowest π^* orbital on the bpy acceptor ligand and the in-plane π^* carbonyl orbitals in the MLCT excited states of *fac*-[Re(4,4′-X_2bpy)$(CO)_3$(4-Etpy)]$^{+}$* (X = CH_3, H, CO_2Et) for X = CH_3 and CO_2Et.

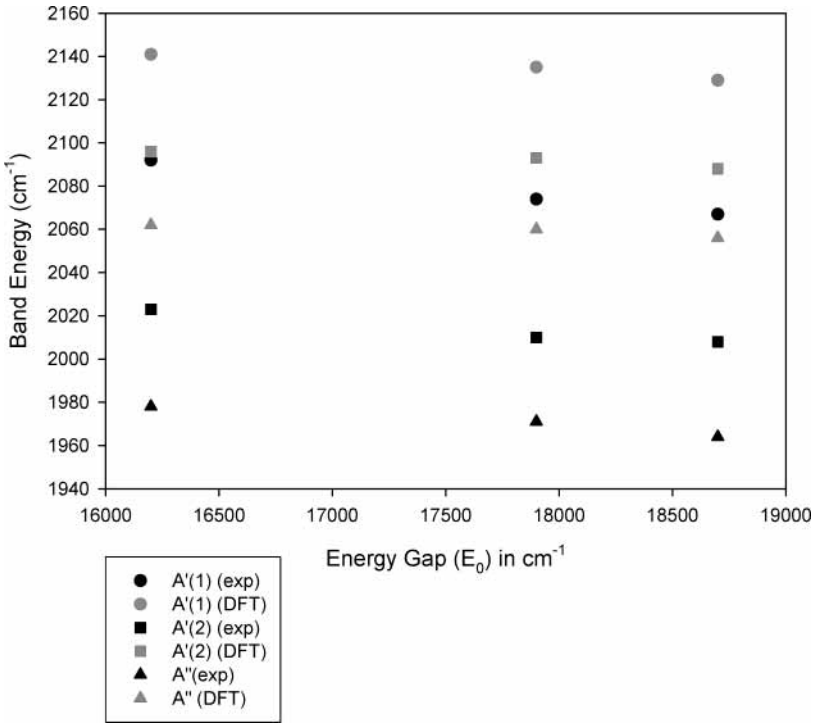

Figure 5. Experimental and calculated band energies for the three carbonyl modes (A′(1), A′(2), and A″) in the lowest MLCT excited states in the series *fac*-[Re(4,4′-X_2bpy)$(CO)_3$(4-Etpy)]$^{+}$* (X = CH_3, H, CO_2Et). The slopes of the plots are mentioned in the text.

solution value is 2.22 eV in acetonitrile at 298 K. TDDFT results for the three states in absorption show similar spacings.[39]

ν(CO) band energies are excellent reporters of even subtle changes in electronic structure in the MLCT excited states. Band energies are sensitive to variations in electron density at the metal, and the high oscillator strengths and convenient spectral range add up to significant experimental advantages for TRIR studies. In the series of Re complexes, multiple factors were identified that contribute to ground-to-excited state ν(CO) shifts. A major factor explaining the large, positive shifts in ν(CO) in the MLCT excited states is the loss of dπ(M)−π^*(CO) back-bonding which accompanies the change in electronic structure from dπ(M)$^6\pi^*$(pp)^0 to dπ(M)$^5\pi^*$(pp)^1.

In the earlier study, systematic variations in ground (gs) and excited state (es) band energies for ν(CO), $\bar{\nu}_{gs}$, $\bar{\nu}_{es}$, and $\Delta\bar{\nu}$ ($\Delta\bar{\nu} = \bar{\nu}_{es} - \bar{\nu}_{gs}$) were observed as the excited-to-ground-state energy gap (E_0) was varied. A variety of electronic interactions was invoked to explain the variations. They included the following points:

(1) The first is variations in dπ(M)−π^*(CO) ground-state back-bonding as revealed by variations in ν(CO) in the series *cis*-[Os(pp)$_2$(CO)(L)]$^{n+}$ (pp = 1,10-phenanthroline (phen) or

2,2′-bipyridine (bpy); L = PPh_3, CH_3CN, pyridine, Cl, or H). In this series, dπ orbital energies and ground state back-bonding are varied systematically with L.

(2) Then there is loss of back-bonding combined with σ(M−CO) bond polarization in the MLCT excited states as inferred from the magnitudes of ground-to-excited-state shifts, $\Delta\bar{\nu}$ ($\Delta\bar{\nu} = \bar{\nu}_{es} - \bar{\nu}_{gs}$) in the series *fac*-[Re(4,4′−X_2bpy)$(CO)_3$(4-Etpy)]-(PF_6) (X = CH_3, H, CO_2Et). While the shifts were large and positive in all cases, $\Delta\bar{\nu}$ was found to *decrease* with increasing energy gap.

(3) This is followed by $\pi^*(pp^{\bullet-})-\pi^*(CO)$ excited state mixing, which provides the orbital basis for mixing $\pi^*(CO)$ and π^*(4,4′-X_2bpy)-based MLCT excited states.

(4) Finally there is dπ(M)−π(pp) excited state mixing, which provides the orbital basis for mixing $\pi\pi^*$ and π^*(4,4′-X_2bpy$^{\bullet-}$)-based MLCT states.

Preliminary DFT results on *fac*-[Re(bpy)$(CO)_3$(4-Etpy)]$^{+}$* were presented previously to aid in the assignments of the ν-(CO) bands in the ground and excited state.[8] In the present study, a more detailed analysis is presented in order to provide additional insight into excited-state structure. The resulting structural changes, transition energies, and ν(CO) shifts calculated for the series *fac*-[Re(4,4′−X_2bpy)$(CO)_3$(4-Etpy)](PF_6) (X = CH_3, H, CO_2Et) provide a wealth of information about MLCT excited-state electronic structure.

Theoretical and Experimental Transition Energies. Calculated gas-phase transition energies, from separate self-consistent field (SCF) calculations on the ground and triplet excited states, and experimental values are listed in Table 2 (in eV). As noted above, E_0 is the $\nu = 0 \rightarrow \nu' = 0$ transition energy in solution based on the single mode approximation. It is related to the free energy of the excited state above the ground state, ΔG^0_{ES}, by

$$\Delta G^0_{ES} = E_0 + \lambda_{0,L} \qquad (2)$$

$\lambda_{0,L}$ is the solvent reorganization energy including low-frequency vibrational modes treated classically.

The theoretical values are shown corrected for zero point energies in column 6 of Table 2. Note that the ground-to-excited-state energy gap increases across the series, [Re(4,4′-(CO_2-Et)$_2$bpy)$(CO)_3$(4-Etpy)]$^+$ < [Re(bpy)$(CO)_3$(4-Etpy)]$^+$ < [Re-(4,4′-$(CH_3)_2$bpy)$(CO)_3$(4-Etpy)]$^+$. This variation is caused by the electronic influence of the 4,4′ substituent on the lowest π^*(bpy) orbital energy. The increase in energy gap is accompanied by an increase in *S*, the electron-vibrational coupling constant, or Huang−Rhys factor derived by emission spectral fitting, for the coupled vibrations treated as an averaged mode. An increase in *S* is indicative of increased distortion on the polypyridyl acceptor ligand in the excited state and, by inference, increased charge-transfer character in the MLCT excited state.[47]

The DFT results verify the trend in energy gap with changes in substituents on the bipyridine ligand, for this series of complexes. The calculated values of the gas-phase zero point corrected energy gap, ΔE(S→T) are greater than the solution experimental values (including $\lambda_{o,L}$) by 0.16 eV on average. This higher gas-phase energy gap points to a loss of solvation energy in the excited state compared to the ground state, a result consistent with the reduced dipole moments predicted by calculation (Table 2). Of course, errors in magnitude may also arise from inadequacies in the functional and basis set as well.

Ground-State Molecular Structure. As shown in Table 6, the bond lengths and angles from the DFT calculations for the three complexes in the ground state are very similar. Inspection of the calculated CO force constants in Tables 3−5 reveals similar values across the series. A very slight trend of increasing CO force constants with decreasing dπ-π^* energy gap (Figure 4) is observed, dimethyl−bpy (35.07 mdyn/Å (A′(1)), 32.89 mdyn/Å (A′(2)), 32.48 mdyn/Å, A″) < bpy (35.15 mdyn/Å (A′-(1)), 33.0 mdyn/Å (A′(2)), 32.57 mdyn/Å, A″) < diester−bpy (35.15 mdyn/Å (A′(1)), 33.06 mdyn/Å (A′(2)), 32.62 mdyn/Å, A″). A slight decrease might have been expected in the CO force constants and a corresponding increase in R(C−O) with increasing electron donating capability of the bpy −X substituent due to increased back-bonding. However, only a slight trend is observed over the range of substituents used and experimental ν(CO) band energies are nearly constant in the ground state across the series.

In the series, the calculated $R(CO_{ax})$ bond lengths are 1.156−1.157 Å with $R(CO_{eq})$ 1.159−1.160 Å. For comparison, the DFT value for R(CO) in free CO is 1.138 Å compared to the experimental value of 1.143 Å when computed with the functional and basis set used in the present work.[40] The lengthening of R(CO) in the metal complex compared to free CO is due to dπ(Re)−π^*(CO) back-bonding to the bound carbonyl. The CO_{eq}−Re−CO_{eq} and CO_{ax}−Re−CO_{eq} bond angles are nearly identical in each complex in the ground state and are close to an idealized octahedral geometry of 90°.

Ground-State Electronic Structure and Vibrational Energies. In the ground state, the symmetry is pseudo-C_{3v} due to the electronic similarity of the 2,2′-bipyridine and 4-ethylpyridine ligands in the local coordination sphere around Re(I). This fact explains the appearance of only two ν(CO) bands in the mid-IR (1900−2200 cm^{-1}). In the spectra a band corresponding to the totally symmetric A_1 mode appears at high energy and a broad band appears at lower energy for the nearly degenerate A′(2) and A″ modes.

The energy factored force field (EFFF) approach has proven very successful in providing information on the geometric and electronic structure of carbonyl containing complexes.[41−43] Detailed EFFF calculations have been carried out on [Re(4,4′-bpy)$_2$$(CO)_3$Cl].[23] The results of this analysis show that the ordering of the ν(CO) bands is A′ > A″ > A′. In contrast, a number of facial tricarbonyl complexes have the ordering of A′ > A′ > A″.[44−46] The current DFT analysis demonstrates the same ordering as the latter studies. This difference suggests that the greater asymmetry around the Re$(CO)_3$ unit for [Re-(4,4′-bpy)$_2$$(CO)_3$Cl] and other electronic effects result in a change in the ordering.

The DFT approach can be viewed as a more complete force field analysis, but it is also an approximation. The EFFF approach has the advantage in that it is semiempirical, and experimental data are used to guide the analysis. However, in the EFFF analysis, it is necessary to estimate a number of intermode couplings. The DFT calculations compute these couplings directly. One real advantage of the DFT approach is that it provides energies and intensities, which can be compared to experimental results. The intensities provide additional information and a further test of the energy ordering.

As noted above, the ground-state experimental ν(CO) band energies are nearly constant through the series. A single band appears near 2035 cm^{-1} and a broad feature consisting of overlapping bands centered near 1927 cm^{-1} (CH_3CN, 298 K). The DFT calculations predict the energy ordering to be A′(1) > A′(2) > A″. The calculated values of the A′(1) bands in the series are 2117, 2120, and 2120 cm^{-1}. There are slight increases in calculated and experimental band energies for the A′(2) and A″ modes as E_0 decreases (Table 1). This presumably is due to

decreased dπ(Re)−π*(CO) back-bonding in the ground state because increased dπ(Re)−π*(4,4′-X_2bpy) mixing increases the dπ(Re)−π*(CO) gap.

Not unexpectedly, the absolute gas-phase energies in the DFT calculations are high (by ∼100 cm^{-1}), but the calculations adequately predict the separations between the A′(1) and nearly degenerate A″ and A′ modes (80 cm^{-1} calculated, 110 cm^{-1} observed).

Tables 3−5 also list reduced masses (μ(amu)), force constants (k (mdyn/Å)), and relative infrared intensities (I_{ir} (KM/mol)). The force constants increase in the order A′(1) > A′(2) > A″, which is the origin of the trend in band energies.

Excited-State Electronic Structure and Vibrational Energies. The DFT results reveal significant changes in molecular and electronic structure between the ground and lowest lying MLCT triplet state. Differences also exist across the series of complexes as the energy gap varies. Figure 2 illustrates the HOMO and LUMO for the ground state of [Re(bpy)$(CO)_3$(4-Etpy)]$^+$. The HOMO is primarily metal-based and transforms as a″. There is significant π*(CO) character and a π contribution from the pyridyl ligand. The LUMO transforms as a′ and is primarily based on the bipyridine. The lowest lying triplet corresponds closely to this HOMO to LUMO excitation and is of A″ symmetry. The orbital plots are consistent with the description of this state as resulting from metal-to-ligand charge-transfer excitation.

There are slight changes in these orbitals if the MLCT state is allowed to relax self-consistently. Figure 3 displays the two natural orbitals, which principally contain the unpaired spin for the triplet A″ SCF solution at its equilibrium geometry. Note that while the a′ symmetry bipyridyl orbital is nearly unchanged from its ground-state counterpart, significant orbital relaxation occurs in the a″ orbital. There is significant migration of electronic amplitude from the metal onto the bipyridyl ligand, leaving much less unpaired spin on the metal. The origin of this effect is a mixing of bipyridyl $\pi \rightarrow \pi^*$ character into the MLCT state through π(X_2-bpy) mixing with the hole in the dπ orbitals.

Several structural changes are evident upon excitation from ground to MLCT excited-state both in bond lengths and bond angles (Table 6). The general trend for all three complexes is a shortening of the R(CO) bond lengths with $R(CO_{ax})$ shortened by about a factor of ∼2 compared to $R(CO_{eq})$. As the CO bonds shorten, R(Re−CO) bonds lengthen, even though the metal is partially oxidized. This structural change is also more pronounced in the axial direction with $R(Re-CO_{ax})$ lengthening by 0.04−0.06 Å. Both structural changes can be attributed to loss of back-bonding in the excited state due to partial oxidation of Re.

The excited-state calculations show that the carbonyl bands retain the same energy ordering in the excited state (A′(1) > A′(2) > A″) with all three bands shifted to higher energy. The absolute calculated excited-state vibrational energies are high (no scaling was used), but energy differences between the ground and excited states are comparable to experimental values (30−40 cm^{-1} calculated; 50 cm^{-1} observed). As illustrated in Figure 5, band energies decrease with increasing energy gap for all three normal modes. From the experimental results, the slopes are -1.0×10^{-2} for A″, -6.3×10^{-3} for A′(2), and -5.4×10^{-3} for A′(1). From the DFT calculations, the slopes are -4.6×10^{-3}, -3.0×10^{-3}, and -2.2×10^{-3}. While the magnitudes of the slopes for the DFT calculated results are approximately half those of the experimental values, relative magnitudes are maintained. In particular, the ratio A′(2)/A″ is nearly the same, ca. 0.6. This comparison demonstrates that the dependence of A′(2) on the energy gap is roughly 60% that of A″.

The shortening of R(CO) and accompanying shift to higher energy of the ν(CO) bands in the excited state is a structural marker for a decrease in dπ(Re)−π*(CO) back-bonding in the excited state. This decrease in back-bonding is expected to occur for all three complexes as the metal center undergoes partial oxidation from Re^{I} to Re^{II} in the MLCT excited state(s). One contribution to the underestimated $\Delta\nu$(CO) values from theory compared to experiment is the neglect of solvation. A dielectric environment would be expected to accentuate the extent of charge transfer by stabilizing charge separation. This effect would lead to an even greater decrease in back-bonding and an accompanying increase in ν(CO).

The shortening of the CO bonds between ground and excited state is paralleled by the monotonic increase in CO force constants for the three modes. For example, for *fac*-[Re(bpy)-$(CO)_3$(4-Etpy)]$^+$, the ground-state force constants, k, are 35.15 (A′(1)), 33.0 (A′(2)), and 32.57 mdyn/Å, (A″). In the excited state, they increase to 35.83 (A′(1)), 34.47 (A′(2)), and 33.37 mdyn/Å, (A″). The increase is in the order: A′(2) > A″ > A′(1). The mode with the largest axial contribution, A′(2), has the largest increase in overall force constant.

Local mode compositions given for the related complex *fac*-[Re(4,4′-bipyridine)$_2(CO)_3$Cl] are shown below, with equatorial (eq) referring to the in-plane CO's and axial (ax) to the perpendicular CO.[23]

$$A'(1) = 0.4717r_{ax}, \quad 0.6235r_{eq} \tag{3}$$

$$A'(2) = 0.8828r_{ax}, \quad 0.3335r_{eq} \tag{4}$$

$$A'' = 0.0r_{ax}, <ep;9q> 0.7071r_{eq} \tag{5}$$

The extent of charge transfer onto the polypyridyl ligand increases with the energy gap as shown by the increase in Huang−Rhys factor, S, from 1.0 to 1.4 in changing −X from $-CO_2Et$ to $-CH_3$. The increase in charge-transfer character across the series leaves $R(CO_{eq})$ unaffected consistent with no significant change in Re−CO back-bonding. By contrast, there is a systematic decrease in $R(Re-CO_{ax})$ from 2.002 to 1.992 Å as E_0 increases. A related trend is seen in $R(Re-N_{bpy})$ in Table 6. The decrease in $R(Re-CO_{ax})$ with increasing E_0 is a consequence of a stronger Re−CO σ-bond interaction due to greater bond polarization. The absence of a variation in R(Re−CO_{eq}) may arise from a compensation effect between enhanced σ-bond polarization and π*(4,4′-bpy)−π*(CO) mixing.

These observations substantiate an earlier suggestion about the origin of the decrease in ν(CO) for the A′(1) and A′(2) excited-state bands as the energy gap is increased, Figure 5. This is not a back-bonding effect. It is instead a σ-bond polarization effect with ν(CO) increasing in energy with the extent of charge transfer. This effect is important for A′(1) and A′(2) which possess $R(Re-CO_{ax})$ character, Figure 1.

There is also experimental evidence in the MLCT excited states for mixing between the lowest π*(4,4′−X_2bpy) level in the acceptor ligand and the in-plane π*(CO) orbitals. The orbital interactions involved are illustrated schematically in the energy level diagram in Figure 4 for $-X = -CH_3$ and $-CO_2Et$. The relative orientations of the orbitals involved in the mixing can be surmised from Figure 1.

π*(4,4′-X_2bpy$^{\bullet-}$)−π*(CO) mixing has the effect of delocalizing the excited electron onto the CO ligands, with the largest

effect in the equatorial CO's in the *x*, *y* plane. The π^*(CO) orbitals for the axial CO ligand are orthogonal to the plane and mix far less.

As shown in Figure 4, the effect is greater for $-X = -CH_3$ because the smaller π^*(4,4′-X_2bpy$^{\cdot -}$)$-\pi^*$(CO) energy gap enhances the degree of mixing. The extent of π^*(4,4′-X_2bpy$^{\cdot -}$)$-\pi^*$(CO) mixing increases in the order $X = CO_2Et < H < CH_3O < CH_3$, as the energy of π^*(4,4′$-X_2$bpy) increases and the π^*(4,4′$-X_2$bpy) -π^*(CO) energy gap decreases.

The importance of π^*(4,4′$-X_2$bpy) -π^*(CO) mixing appears in [Re(dppz)$(CO)_3(PPh_3)]^+$ and [Re(Me_2dppz)$(CO)_3$(4-Etpy)]$^+$ (dppz is dipyrido[3,2-*a*:2′,3′-*c*]phenazine; Me_2dppz is dimethyldipyrido[3,2-*a*:2′,3′*c*]phenazine), which have a lowest-lying, ligand-based $\pi\pi^*$ excited state.[11] In these cases, the ν(CO) bands shift slightly to lower energy in the excited states due to π^*-(dppz$^{\bullet -}$)$-\pi^*$(CO) mixing.[11]

The DFT calculations are consistent with this interpretation. In the excited state they predict a decrease in the OC−Re−CO bond angle to 86.4° for the equatorial CO's compared to 90.5° in the ground state in order to maximize π^*(4,4′$-X_2$bpy$^{\bullet -}$)$-\pi^*$(CO) overlap. The increase in equatorial-axial bond angles from 90.3 and 90.9 in the ground state to 91.4 and 91.9 in the excited state can be attributed to enhanced electron−electron repulsion due to buildup of charge in the equatorial CO's.

For the A″ normal mode, the equatorial carbonyls move in an out-of-phase fashion, Figure 1. The DFT calculations suggest that the OC−Re−CO bond angle change should cause a decrease in transition dipole moment and band intensity for the A″ ν(CO) band compared to A′(2). For A′(2) the equatorial carbonyls move in-phase, and the decrease in OC−Re−CO angle causes a decrease in the magnitude of the transition dipole moment. The DFT calculations predict an intensity ratio of 1:3 A′(2)/A″. This provides an explanation for the common observation that the intensity of the ~ 2010 cm^{-1} band is always greater than the band near 1965 cm^{-1} by about 1:3.

Experimentally, the magnitude of $\Delta\bar{\nu}$ and its variation with E_0 are mode-specific with A′(2) varying from 80 to 88 cm^{-1}, A″ from 31 to 45 cm^{-1}, and A′(1) from 26 to 54 cm^{-1}. This can also be explained by invoking π^*(4,4′$-X_2$bpy$^{\bullet -}$)$-\pi^*$(CO) mixing given the local mode compositions of the ν(CO) bands. The A′(1) and A″ modes have significant contributions from the equatorial carbonyls which dominate π^*(4,4′$-X_2$bpy$^{\bullet -}$)$-\pi^*$(CO) mixing. This increases electron density in π^*(CO), decreases CO force constants and band energies, and makes the infrared bands for these modes more responsive to variations in −X.

A′(2) includes significant axial character and is less influenced by π^*(4,4′$-X_2$bpy$^{\bullet -}$)$-\pi^*$(CO) mixing and in-plane delocalization. This result explains the large value of $\Delta\bar{\nu}$ and the small variations with −X. For A′(2), the magnitude of $\Delta\bar{\nu}$ is dictated largely by loss of dπ(Re)$-\pi^*$(CO) back-bonding and σ(Re−CO) bond polarization in the excited states. π^*(4,4′$-X_2$bpy$^{\bullet -}$)$-\pi^*$(CO) mixing is relatively unimportant.

Acknowledgment. This work was performed at Los Alamos National Laboratory, operated by the University of California for U. S. Department of Energy under Contract No. W-7405-ENG-36. The Laboratory Directed Research and Development Program provided funding to J.R.S. (Project 20020222ER) and R.L.M. for this work. D.M.D. also thanks the Director's Funded Postdoctoral Fellowship Program at Los Alamos National Laboratory for support.

References and Notes

(1) Demas, J.; DeGraff, B. *J. Chem. Educ.* **1997**, *74*, 690−695.
(2) Kneas, K.; Xu, W.; Demas, J.; DeGraff, B.; Zipp, A. *J. Fluoresc.* **1998**, *8*, 295−300.
(3) Keefe, M.; Slone, R.; Hupp, J.; Czaplewski, K.; Snurr, R.; Stern, C. *Langmuir* **2000**, *16*, 3964−3970.
(4) Lam, M.; Lee, D.; Man, K.; Lau, C. *J. Mater. Chem.* **2000**, *10*, 1825−1828.
(5) Sun, S.; Lees, A. *Coord. Chem. Rev.* **2002**, *230*, 171−192.
(6) Costa, I.; Montalti, M.; Pallavicini, P.; Perotti, A.; Prodi, L.; Zaccheroni, N. *J. Organomet. Chem.* **2000**, *594*, 267−273.
(7) Petrovich, V.; Haurylau, M.; Volchek, S. *Sens. Actuators A: Phys.* **2002**, *99*, 45−48.
(8) Dattelbaum, D. M.; Omberg, K. M.; Schoonover, J. R.; Meyer, T. J. *Inorg. Chem.* **2001**, *41*, 6071−6979.
(9) Abbott, L. C.; Arnold, C. J.; Ye, T.-Q.; Gordon, K. C.; Perutz, R. N.; Hester, R. E.; Moore, J. N. *J. Phys. Chem. A* **1998**, *102*, 1252−1260.
(10) Schoonover, J. R.; Bignozzi, C. A.; Meyer, T. J. *Coord. Chem. Rev.* **1997**, *165*, 239−266.
(11) Schoonover, J. R.; Strouse, G. F.; Dyer, R. B.; Bates, W. D.; Chen, P.; Meyer, T. J. *Inorg. Chem.* **1996**, *35*, 273−274.
(12) Schoonover, J. R.; Strouse, G. F.; Omberg, K. M.; Dyer, R. B. *Comments Inorg. Chem.* **1996**, *18*, 165.
(13) Schoonover, J. R.; Gordon, K. C.; Argazzi, R.; Woodruff, W. H.; Peterson, K. A.; Bignozzi, C. A.; Dyer, R. B.; Meyer, T. J. *J. Am. Chem. Soc.* **1993**, *115*, 10996−10997.
(14) Stufkens, D. J.; Vlcek, A. *Coord. Chem. Rev.* **1998**, *177*, 127−179.
(15) Glyn, P.; George, M. W.; Hodges, P. M.; Turner, J. J. *J. Chem. Soc., Chem. Commun.* **1989**, 1655.
(16) Turner, J. J.; George, M. W.; Johnson, F. P. A.; Westwell, J. R. *Coord. Chem. Rev.* **1993**, *125*, 101.
(17) Rossenaar, B. D.; Stufkens, D. J.; Vlcek, A. J. *Inorg. Chem.* **1996**, *35*, 2902−2909.
(18) Kober, E. M.; Meyer, T. J. *Inorg. Chem.* **1984**, *23*, 3877−3886.
(19) Crosby, G. A. *Acc. Chem. Res.* **1975**, *8*, 231−238.
(20) Striplin, D. R.; Crosby, G. A. *Chem. Phys. Lett.* **1994**, *221*, 426−430.
(21) Vlcek, A.; Grevels, F. W.; Snoeck, T. L.; Stufkens, D. J. *Inorg. Chim. Acta* **1998**, *278*, 83−90.
(22) Braterman, P. S. *Metal Carbonyl Species*; Academic Press: London, 1975.
(23) Gamelin, D. R.; George, M. W.; Glyn, P.; Grevels, F.-W.; Johnson, F. P. A.; Klotzbucher, W.; Morrison, S. L.; Russell, G.; Schaffner, K.; Turner, J. J. *Inorg. Chem.* **1994**, *33*, 3246.
(24) McQuillan, G. P.; McKean, D. C.; Long, C.; Morrisson, A. R.; Torto, I. *J. Am. Chem. Soc.* **1986**, *108*, 863−871.
(25) Moigno, D.; Pavel, I.; Kiefer, W.; Jehle, H.; Malisch, W. *J. Organomet. Chem.* **2002**, *648*, 155−163.
(26) Schettino, V.; Pagliai, M.; Cardini, G. *J. Phys. Chem. A.* **2002**, *106*, 1815−1823.
(27) Sun, G. Y.; Kertesz, M. *J. Phys. Chem. A.* **2002**, *106*, 6381−6386.
(28) Wu, D. Y.; Ren, B.; Jiang, Y. X.; Xu, X.; Tian, Z. Q. *J. Phys. Chem. A.* **2002**, *106*, 9042−9052.
(29) Moroni, L.; Gellini, C.; Salvi, P. R.; Liu, C.-J.; Vogel, E. *J. Phys. Chem. A.* **2002**, *106*, 6554−6562.
(30) Nakata, M.; Kudoh, S.; Takayanagi, M.; Ishibashi, T.-A.; Kato, C. *J. Phys. Chem. A.* **2000**, *104*, 11304−11309.
(31) Ong, S. Y.; Zhu, P. Z.; Poon, Y. F.; Leung, K. H.; Fang, W. H.; Phillips, D. L. *Chem.—Eur. J.* **2002**, *8*, 2163−2171.
(32) Martin, C. B.; Tsao, M.-L.; Hadad, C. M.; Platz, M. S. *J. Am. Chem. Soc.* **2002**, *124*, 7226−7234.
(33) Worl, L. A.; Duesing, R.; Chen, P.; Della Ciana, L.; Meyer, T. J. *J. Chem. Soc., Dalton Trans.* **1991**, 849−858.
(34) Chen, P.; Duesing, R.; Graff, D. K.; Meyer, T. J. *J. Phys. Chem.* **1991**, *95*, 5850−5858.
(35) Chen, P.; Palmer, R. A. *Appl. Spectrosc.* **1997**, *51*, 580−583.
(36) Becke, A. D. *J. Chem. Phys.* **1993**, *98*, 1372.
(37) Frisch, M. J.; Trucks, G. W.; Schlegel, H. B.; Scuseria, G. E.; Robb, M. A.; Cheeseman, J. R.; Zakrzewshi, V. G.; Montgomery Jr., J. A.; Stratmann, R. E.; Burant, J. C.; Dapprich, S.; Millam, J. M.; Daniels, A. D.; Kudin, K. N.; Strain, M. C.; Farkas, O.; Tomasi, J.; Barone, V.; Cossi, M.; Cammi, R.; Mennucci, B.; Pomelli, C.; Adamo, C.; Clifford, S.; Ochterski, J.; Petersson, G. A.; Ayala, P. Y.; Cui, Q.; Morokuma, K.; Malick, D. K.; Rabuck, A. D.; Raghavachari, K.; Foresman, J. B.; Cioslowski, J.; Ortiz, J. V.; Baboul, A. G.; Stefanov, B. B.; Liu, G.; Liashenko, A.; Piskorz, P.; Komaroni, I.; Gomparts, R.; Martin, R. L.; Fox, D. J.; Keith, T.; Al-Laham, M. A.; Peng, C. Y.; Wong, M. W.; Andres, J. L.; Gonzolez, C.; Head-Gordon, M.; Replogle, E. S.; Pople, J. A. Gaussian Inc.: Pittsburgh, PA, 1998.

(38) Hay, P. J.; Wadt, W. R. *J. Chem. Phys.* **1995**, *82*, 299.
(39) Martin, R. L. *J. Chem. Phys.* **2003**, *118*, 4775.
(40) Huber, K. P.; Herzberg, G. P. *Constants of Diatomic Molecules*; Van Nostrand Reinhold: New York, 1970.
(41) George, M. W.; Turner, J. J. *Coord. Chem. Rev.* **1998**, *177*, 201−217.
(42) Burdett, J. K.; Poliakoff, M.; Timney, J. A.; Turner, J. J.; et.al. *Inorg. Chem.* **1978**, *17*, 948−952.
(43) Cotton, F. A.; Kraihanzel, C. S. *J. Am. Chem. Soc.* **1962**, *84*, 4432−4438.
(44) Wuyts, L. F.; Van Der Kelen, G. P. *Inorg. Chim. Acta* **1977**, *23*, 19−22.
(45) Staal, L. H.; Oskam, A.; Vrieze, K. *J. Organomet. Chem.* **1979**, *170*, 235.
(46) Brisdon, B. J.; Edwards, D. A.; White, J. W. *J. Organomet. Chem.* **1978**, *156*, 427−437.
(47) Kober, E. M.; Caspar, J. V.; Lumpkin, R. S.; Meyer, T. J. *J. Phys. Chem.* **1986**, *90*, 3722−3734. Claude, J. P.; Meyer, T. J. *J. Phys. Chem.* **1995**, *99*, 51−54.